IEEE Access
Multidisciplinary | Rapid Review | Open Access Journal

Received May 28, 2021, accepted June 25, 2021, date of publication July 2, 2021, date of current version July 9, 2021.

Digital Object Identifier 10.1109/ACCESS.2021.3094160

Characteristic Impedance Adjustment of Thin-Metal Mesh Transmission Lines for mmWave Display-Integrated Antennas

JIN MYEONG HEO[1], EUN JIN SUNG[2], JAE KYOUNG KIM[2], AND GANGIL BYUN[1], (Member, IEEE)

[1]School of Electrical Engineering, Ulsan National Institute of Science and Technology (UNIST), Ulsan 44919, South Korea
[2]Samsung Display Company Ltd., Kiheung 17113, South Korea

Corresponding author: Gangil Byun (byun@unist.ac.kr)

This work was supported by Samsung Display Company, Co., Ltd. and the National Research Foundation of Korea (NRF) grant funded by the Korea government(MSIT) (NRF-2021R1C1C1012955).

.

ABSTRACT This paper proposes four methods and empirical formulas of adjusting characteristic impedances for thin-metal mesh transmission lines. The characteristic impedances are discretely adjusted by changing the number and the size of unit meshes, which provides macro-tuning capability, and the discrete values can be tuned more precisely by varying the thin-metal line width and the aspect ratio of mesh geometry. The validity of proposed methods is confirmed by full-wave numerical simulations, and the simulated impedance variations are well-described by our empirical formulas. For further verifications, 26 distinguished samples of thin-metal mesh transmission lines and a 28-GHz thin-metal mesh antenna are fabricated, and their characteristics are measured in millimeter-wave spectrums. The measured results confirm that the proposed methods and empirical formulas can provide accurate and more flexible design rules for impedance adjustment, which allows potential advances in display-integrated antenna applications.

INDEX TERMS Display-integrated, thin-metal mesh, optically transparent, characteristic impedance.

I. INTRODUCTION

Antennas with broader bandwidths are desirable for mobile phones to enable higher data rates in the fifth-generation (5G) millimeter-wave (mmWave) communications [1]–[5]. Since higher-band spectrums exhibit substantial space losses due to their extremely short wavelengths, mobile phones with 5G connectivity are often accompanied with a number of antenna elements to increase the directivity toward base stations [6]–[8]. However, the space available for the antenna elements tends to be smaller in mobile phones because of increasing demands on narrower bezels with larger screens [9], [10]. Thus, various efforts have been initiated to integrate antennas into a display panel by making the geometry optically transparent [11]–[15]. One of the famous approaches is the use of indium tin oxide (ITO) that guarantees high transparency of above 80% [16]–[20]; however, its low conductivity ($\sigma = 2.88 \times 10^5$, [16]) significantly reduces the antenna efficiency [17], [21], [22]. Another famous approach is the use of thin-metal mesh lines, whose transparency is similar to that of ITO [22]–[26]. This approach has gained popularity because of its high effective conductivity of greater than $\sigma = 1.85 \times 10^7$ S/m, which results in better antenna efficiency [11], [22], [23]. Hence in [11], a microstrip patch antenna and its feeding line have been implemented as thin-metal meshes that are made of Ag-alloy to achieve optical transparency of 88%. Despite this successful integration, impedance matching characteristics, i.e., reflection coefficients and bandwidths, are excessively distorted in measured data. This is due to lack of in-depth considerations on characteristic impedances of thin-metal mesh transmission lines having more complex design parameters, e.g., mesh shape, mesh size, thin-metal line width, and metal thickness. Note that these parameters should be carefully tuned by considering geometric restrictions of display panels, such as pixel sizes, arrangement of light emitting diodes (LED), and fabrication tolerances of organic and inorganic compositions [27]. In addition, due to the fact that the width

The associate editor coordinating the review of this manuscript and approving it for publication was Raghvendra Kumar Chaudhary.

This work is licensed under a Creative Commons Attribution 4.0 License. For more information, see https://creativecommons.org/licenses/by/4.0/

and thickness of thin-metal lines are usually similar to or less than the skin depth, there is a drastic change in ohmic losses, which leads to unexpected degradations in radiation efficiency and gain [28]. Therefore, in-depth studies on characteristic impedances of thin-metal mesh transmission lines are required to enable accurate modeling of display-integrated antennas with a broad bandwidth and high gain in such complex design restrictions.

Here, four methods of adjusting characteristic impedances are proposed with empirical formulas for thin-metal mesh transmission lines. The proposed formulas are defined by introducing a correction term with a filling factor and are generalized for rhombus meshes by considering all possible combinations of geometric parameters. Methods 1 and 2 vary the number and the size of unit meshes to provide macro-tuning capability as discrete values, and Methods 3 and 4 are effective to precisely tune those discrete impedances by changing width of thin-metal lines and the aspect ratio of rhombus. The accuracy of our empirical formulas is validated by comparing with full-wave numerical simulations for different geometric parameters of the four methods. Then, 26 distinguished samples of thin-metal mesh transmission lines are fabricated by photolithography, and their two-port scattering parameters are measured in a semi-anechoic chamber by using a vector network analyzer (VNA). Note that characteristic impedances are obtained from the measured scattering parameters by subtracting the properties of grounded coplanar waveguides (GCPWs) at two ports. For further validation, the knowledge obtained above is extended to a thin-metal mesh antenna operating at 28 GHz to confirm the modeling accuracy in comparison with measured antenna characteristics. The results demonstrate that the four methods are effective to achieve macro- and micro-tuning capabilities, and the proposed formulas provide accurate computations of characteristic impedances for such complex design parameters of thin-metal mesh transmission lines.

The paper is organized as follows: after the introduction of Section I, the empirical formulas will be explained with the four methods in Section II. In Section III, measured results of thin-metal mesh transmission lines and an example display-integrated antenna will be presented, then the conclusions will be followed in Section IV.

II. CHARACTERISTIC IMPEDANCE ADJUSTMENT

A. EMPIRICAL FORMULAS

Fig. 1 shows a conceptual illustration of display-integrated thin-metal mesh transmission lines printed on a transparent film, and optically clear adhesive (OCA) is used to attach the antenna film to a display panel that has a cathode layer at its top face. Through our two-year research experience on this topic, we discovered that electromagnetic waves in mmWave spectrums are barely penetrated through the panel due to its lossy material properties and metallic patterns of the cathode layer. So, we simplified the substrate of thin-metal mesh transmission lines as an equivalent homogeneous medium to provide in-depth analyses by focusing on

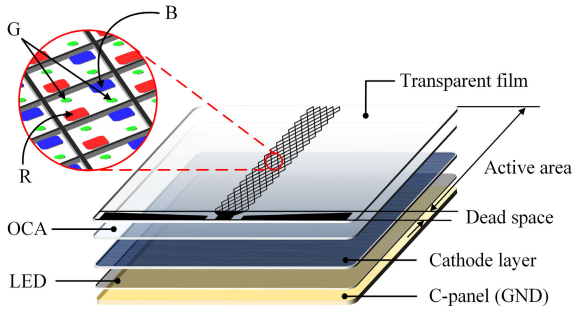

FIGURE 1. Concept of thin-metal mesh transmission line for display-integrated antennas.

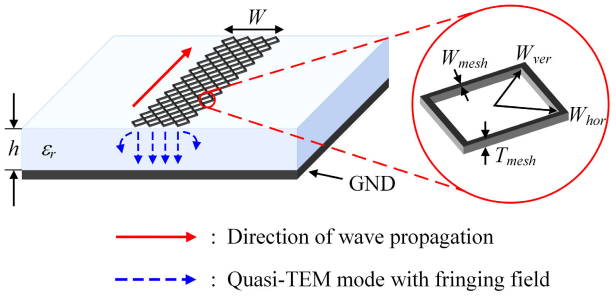

FIGURE 2. Design and geometric parameters of thin-metal mesh transmission lines.

geometric parameters without interactions with other display layers.

Fig. 2 illustrates a simplified design of thin-metal mesh transmission lines with their geometric parameters. The rhombus size is determined by W_{ver} and W_{hor}, and these parameters define the ratio $R_{mesh} = W_{ver}/W_{hor}$. The trace width W, which is the width of transmission lines in the transverse direction, is mainly adjusted by changing the number of rhombus meshes, N_{mesh}. The thin-metal line has width W_{mesh} and thickness T_{mesh}, and the patterns are printed on a substrate with relative permittivity ε_r and loss tangent tan δ. As an initial design guideline, we use a unit mesh of each RGB pixel to have $W_{ver} = 60\ \mu$m, $W_{hor} = 30\ \mu$m, and $R_{mesh} = 2$, which can be changed for different pixel information. The transparent film ($\varepsilon_r = 2.34$, tan $\delta = 0.0006$) is used as a substrate with thickness $h = 100\ \mu$m, and a copper ground with a metal thickness of 60 μm is attached at the bottom face. By considering the available fabrication capability, the metallic patterns are designed to have restrictions of $T_{mesh} = 1\ \mu$m and $W_{mesh} \geq 1\ \mu$m, and the thin-metal mesh lines are modeled as three-dimensional cuboids for more accurate impedance estimations in full-wave numerical simulations.

Fig. 3 presents a top view with additional parameters that are required to define our empirical formulas. A unit area, A_{unit}, contains a row of N_{mesh} rhombus meshes, and there are rhombus-shaped intersections between meshes, as specified by darker grey. The size of intersections, i.e., d_{hor} and d_{ver}, can be written as

$$d_{hor} = W_{mesh}\frac{\sqrt{1+(W_{hor}/W_{ver})^2}}{2} \tag{1}$$

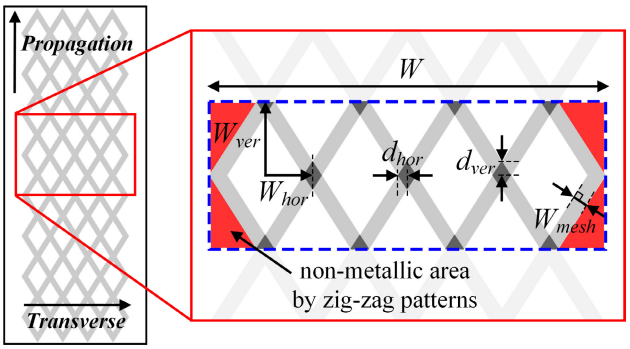

FIGURE 3. Top view of the thin-metal mesh lines with additional parameters. The region inside the boundary of blue-dotted lines is defined as unit area, and the gray lines indicate metallic area.

$$d_{ver} = W_{mesh}\frac{\sqrt{1+(W_{ver}/W_{hor})^2}}{2} \tag{2}$$

and the trace width W is expressed by

$$W = 2(N_{mesh}W_{hor} + d_{hor}) \tag{3}$$

In the extreme condition that the metallic line covers the entire rhombus area like a solid microstrip line, d_{hor} and d_{ver} become identical with W_{hor} and W_{ver}, respectively, and thus, W_{mesh} is restricted to

$$W_{mesh} \le \frac{2W_{hor}W_{ver}}{\sqrt{W_{hor}^2 + W_{ver}^2}}. \tag{4}$$

The filling factor ρ is defined as the proportion of metallic area, A_{metal}, within the unit area and is expressed as

$$\rho = \frac{2N_{mesh}(W_{hor}d_{ver} + W_{ver}d_{hor} - d_{hor}d_{ver}) + d_{hor}d_{ver}}{W \times W_{ver}}. \tag{5}$$

By applying the upper bound of W_{mesh} in (4), (5) reduces to

$$\rho = \frac{2N_{mesh}+1}{2(N_{mesh}+1)}, \tag{6}$$

which implies that ρ converges to one, i.e., the solid line, as N_{mesh} goes to infinity. Fig. 4 shows variations of ρ according to N_{mesh} for different W_{mesh}. It is assumed that the unit mesh has the initial design of $W_{ver} = 60\ \mu$m and $W_{hor} = 30\ \mu$m, then, the upper bound in (4) gives $W_{mesh} = 53.66\ \mu$m. As N_{mesh} becomes greater, ρ tends to increase; however, it is converged to lower values for smaller W_{mesh}. The non-linear region corresponds to the effective range of characteristic impedances from 52 Ω to 129 Ω, i.e., between 60 μm and 420 μm. Note that this non-linear variation occurs because rhombus-shaped pixels create zigzag patterns along the edges of transmission lines, which can be distinguished from the square mesh case in [29]. This filling factor ρ also defines transparency as $T = 1 - \rho$ and plays a key role in our empirical formulas to characterize electromagnetic properties

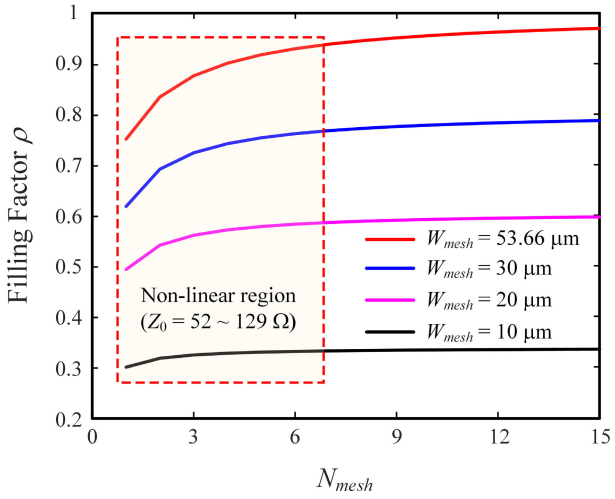

FIGURE 4. Filling factor ρ according to the number of rhombus meshes (N_{mesh}) with different W_{mesh}.

of thin-metal mesh transmission lines. The effective dielectric constant of a conventional solid microstrip line is [30]

$$\varepsilon_{eff}^{solid} = \frac{\varepsilon_r+1}{2} + \frac{\varepsilon_r-1}{2}\left(1+12\frac{h}{W}\right)^{-0.5} \tag{7}$$

and can be modified for the mesh transmission line with the filling factor ρ as [29]

$$\varepsilon_{eff}^{mesh} = \frac{\varepsilon_r+1}{2} + \frac{\varepsilon_r-1}{2}\left(1+12\frac{h\sqrt{\rho}}{W}\right)^{-0.5}. \tag{8}$$

Then, the characteristic impedance of the mesh transmission line, i.e., Z_0^{mesh}, is defined by adding a correction term associated with ρ ($Z_0^{correct}$) to that of the conventional solid microstrip line (Z_0^{solid}), as written by

$$Z_0^{mesh} = Z_0^{solid} + Z_0^{correct}, \tag{9}$$

where the correction term is empirically found as

$$Z_0^{correct} = \frac{0.46}{\sqrt{\varepsilon_{eff}^{mesh}}\rho^{1.35}}\left(\frac{h}{W}\right)^{0.75}, \frac{W_{mesh}}{\delta} < 3.3 \tag{10}$$

$$Z_0^{correct} = \frac{13}{\sqrt{\varepsilon_{eff}^{mesh}}\rho^{0.45}}\left(\frac{h}{W}\right)^{0.75}, \frac{W_{mesh}}{\delta} \ge 3.3 \tag{11}$$

and should be splitted into two expressions by considering the ratio of W_{mesh} to skin depth δ. This is because there is a drastical increase of ohmic losses when the ratio is less than 3.3. For example, since the skin depth of copper at 28 GHz is about $\delta = 0.39\ \mu$m, W_{mesh} of copper lines with conductivity $\sigma = 5.8 \times 10^7$ should be greater than 1.287 μm to prevent significant increase of ohmic losses that cause unexpected distortions in radiation efficiency and gain. Note that the contribution of $Z_0^{correct}$ diminishes, i.e., Z_0^{mesh} is identical with Z_0^{solid}, when W is large enough. In the following section, the accuracy and the universality of the proposed formulas will be validated by comparing with simulated data obtained from full-wave numerical analyses.

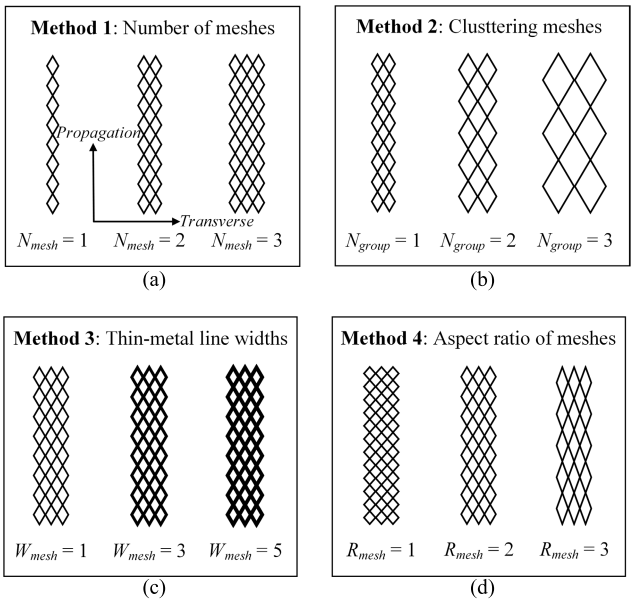

FIGURE 5. Methods for adjusting Z_0 of thin-metal mesh transmission lines. Change of (a) the number of rhombus meshes, (b) the number of clustering meshes, (c) thin-metal line widths and (d) aspect ratio of meshes.

B. METHODS OF ADJUSTING CHARACTERISITIC IMPEDANCES

Fig. 5 shows the proposed four methods to adjust characteristic impedances of thin-metal transmission lines. Method 1 varies the number of rhombus meshes, N_{mesh}, in the transverse direction by maintaining the unit mesh size. Method 2 changes the number of clustering meshes, N_{group}, to form a larger unit mesh, so that the number of pixels included in each clustered mesh increases as the square of N_{group}. Methods 3 and 4 adjust characteristic impedances using W_{mesh} and R_{mesh}, respectively, and are effective to fine-tune the discrete values of Methods 1 and 2.

Figs. 6 and 7 present variations of characteristic impedances that are adjusted by the four methods. Simulated values obtained from full-wave commercial software, Ansys HFSS, are specified by solid lines and are compared with calculated values of the empirical formulas, as indicated by dashed lines. Fig. 6(a) shows variations of characteristic impedances, Z_0, of both solid microstrip and thin-metal mesh transmission lines according to W. Both solid and mesh lines show decreasing tendency of Z_0 as W increases, and Z_0 of the mesh lines is determined as discrete values because of N_{mesh} in (3). In addition, the mesh lines maintain consistently greater Z_0 compared to the solid line, which implies that W of mesh lines should be greater than that of solid lines to have the same Z_0. Note that the deviation between the two lines becomes smaller for larger trace widths, which is also reflected in $Z_0^{correct}$ of the proposed formulas. Fig. 6(b) exhibits variations of Z_0 based on Method 2. The unit mesh size is scaled by varying N_{group}, which is also associated with ρ. As N_{group} increases, Z_0 tends to be greater, because, as discussed in Section II-A, smaller ρ results in greater

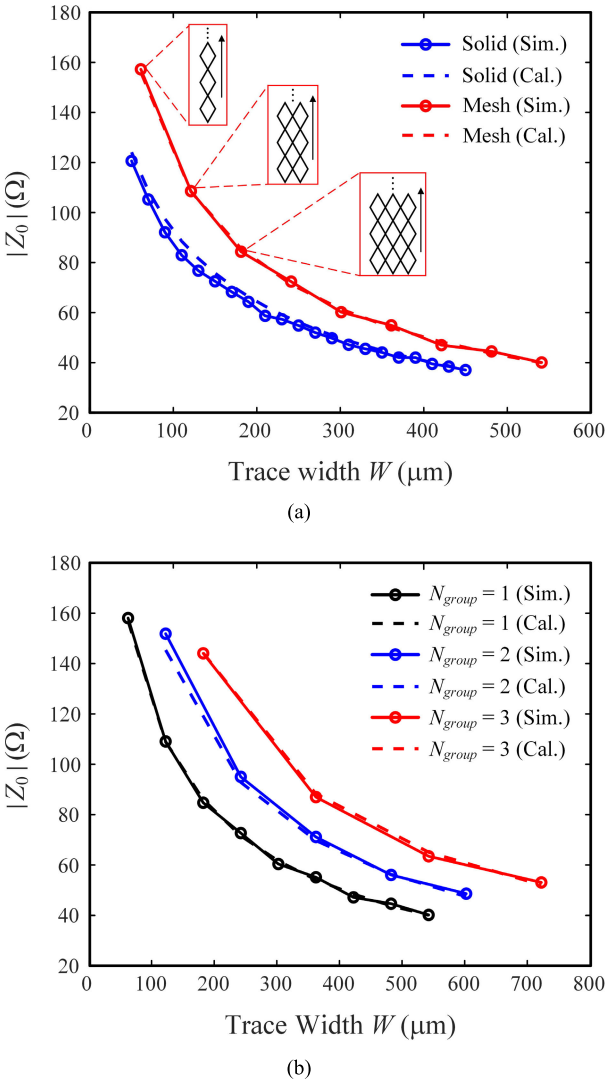

FIGURE 6. Simulated and calculated variation of Z_0 of thin-metal mesh transmission lines according to trace width W for (a) Method 1 (fixing $N_{group} = 1$; $W_{mesh} = 1$ μm; $R_{mesh} = 2$) and (b) Method 2 (fixing $W_{mesh} = 1$ μm; $R_{mesh} = 2$).

contribution of $Z_0^{correct}$. It can be seen that the proposed formulas are capable of predicting accurate Z_0 for various ρ that can be adjusted by N_{mesh} and N_{group}. In addition, the interval between discrete values becomes narrower for a smaller size of unit meshes; however, the mesh size is often restricted to integer multiples of pixel sizes. Thus, to give more design freedom of fine-tuning Z_0, W_{mesh} and R_{mesh} are considered as important design parameters in Methods 3 and 4, respectively. Fig. 7(a) presents variations of Z_0, when W_{mesh} is varied from 1 μm to 7 μm. Since the change of W_{mesh} results in different ρ, Method 3 provides fine-tuning capability with the maximum Z_0 deviation of 19 Ω when $W/h < 1$. This deviation reduces to a few ohms as W increases, because the contribution of ρ in $Z_0^{correct}$ becomes smaller than that of W. Fig. 7(b) shows Z_0 variations according to R_{mesh}, which is adjusted by W_{ver} for a fixed value of $W_{hor} = 30$ μm. Similarly, ρ is also scaled by R_{mesh}, so, Method 4 exhibits

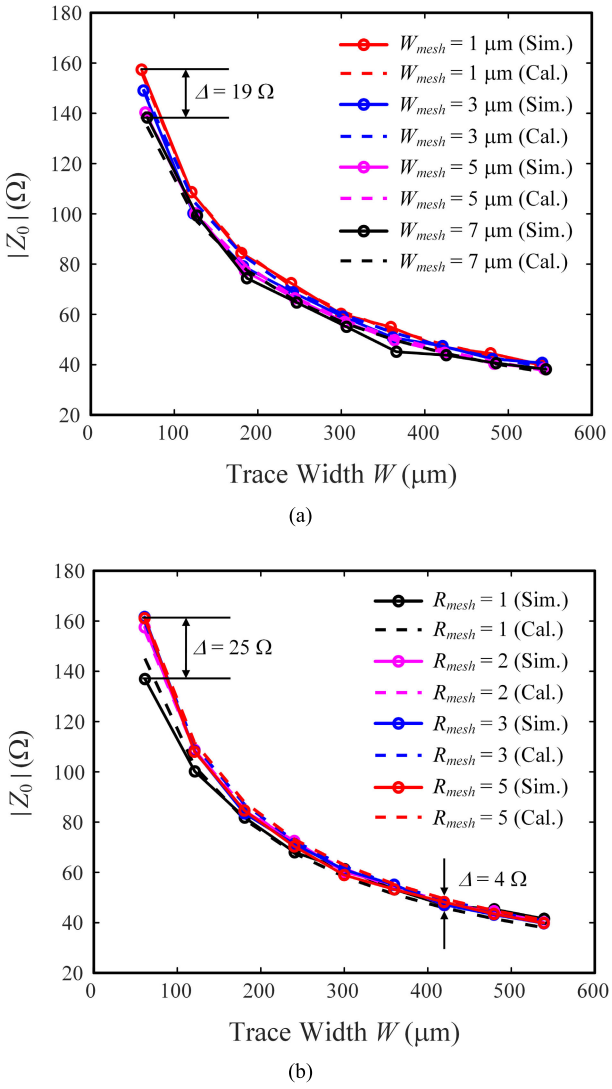

FIGURE 7. Simulated and calculated variation of Z_0 of thin-metal mesh transmission lines according to trace width W for (a) Method 3 (fixing $N_{group} = 1$; $R_{mesh} = 2$) and (b) Method 4 (fixing $N_{group} = 1$; $W_{mesh} = 1$ μm).

the maximum Z_0 deviation of 25 Ω at $W = 60$ μm, and this is reduced to 4 Ω at $W = 420$ μm.

III. FABRICATION AND MEASUREMENT

A. FABRICATED THIN-METAL MESH TRANSMISSION LINES

To verify the feasibility of the proposed four Methods, 26 distinguished samples of thin-metal mesh transmission lines are fabricated by the photolithography [31]. The fabricated dimensions are verified by using an optical microscope from Nikon LV100ND, as shown in Fig. 8(a). The fabricated samples consist of 50-Ω GCPWs, transition and thin-metal mesh microstrip lines as specified in Fig. 8(b). Fig. 9 provides example microscopic views of the four methods, and the fabricated dimensions exhibit geometric error of less than 4.38%, which is acceptable to distinguish parametric changes of the four methods.

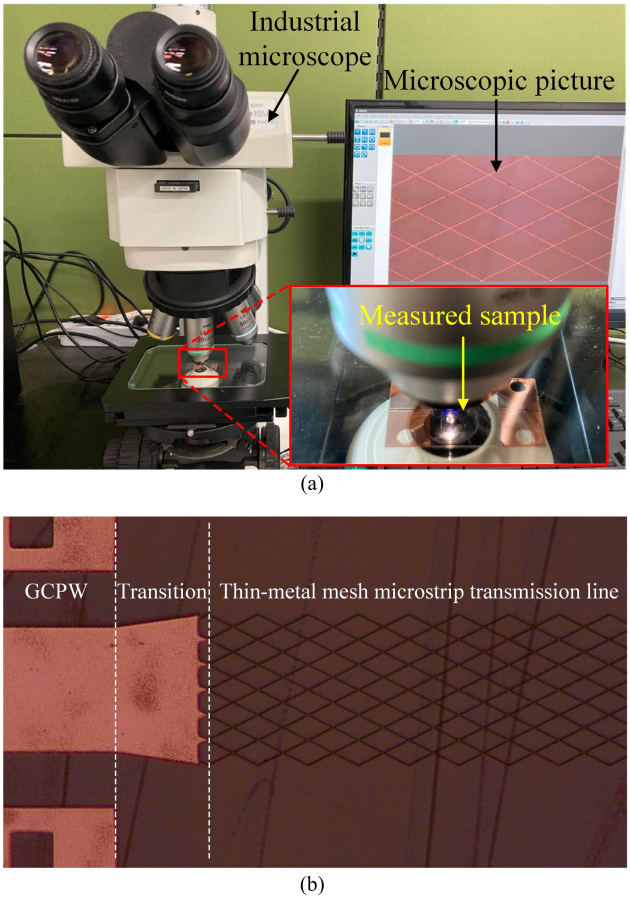

FIGURE 8. Fabricated samples of thin-metal mesh transmission lines and measurement by microscope. (a) Measurement set-up for microscopic observations. (b) Photograph of samples pictured by microscope.

B. MEASUREMENT OF CHARACTERISTIC IMPEDANCES

The characteristic impedances of fabricated samples are measured using an Anritsu MS46122B two-port VNA as shown in Fig. 10. A copper tape with 60-μm thickness is attached to the bottom face of each fabricated sample and is electrically connected to the top ground of 50-Ω GCPWs through end-launch connectors.

Fig. 11 presents an equivalent transmission line model of the fabricated sample that is represented by five series segments of transmission lines with different Z_0 and propagation constant β. The characteristic impedances of the GCPWs are represented by $Z_0^{(0)}$ and $Z_0^{(4)}$, and those of impedance transformers are denoted as $Z_0^{(1)}$ and $Z_0^{(3)}$. The propagation constants and lengths of the five segments are given by β_i and l_i, respectively, for $i = 0, 1, \ldots, 4$. Then, the input impedances at different reference planes, $Z_{in}^{(i+1)}$, are calculated as [30]

$$Z_{in}^{(i+1)} = Z_0^{(i)} \frac{Z_{in}^{(i)} + jZ_0^{(i)} \tan(\beta_i l_i)}{Z_0^{(i)} + jZ_{in}^{(i)} \tan(\beta_i l_i)} \tag{12}$$

and a recursive calculation from $i = 0$ leads to $Z_{in}^{(5)}$, which is the input impedance at Port 1 with six unknowns of

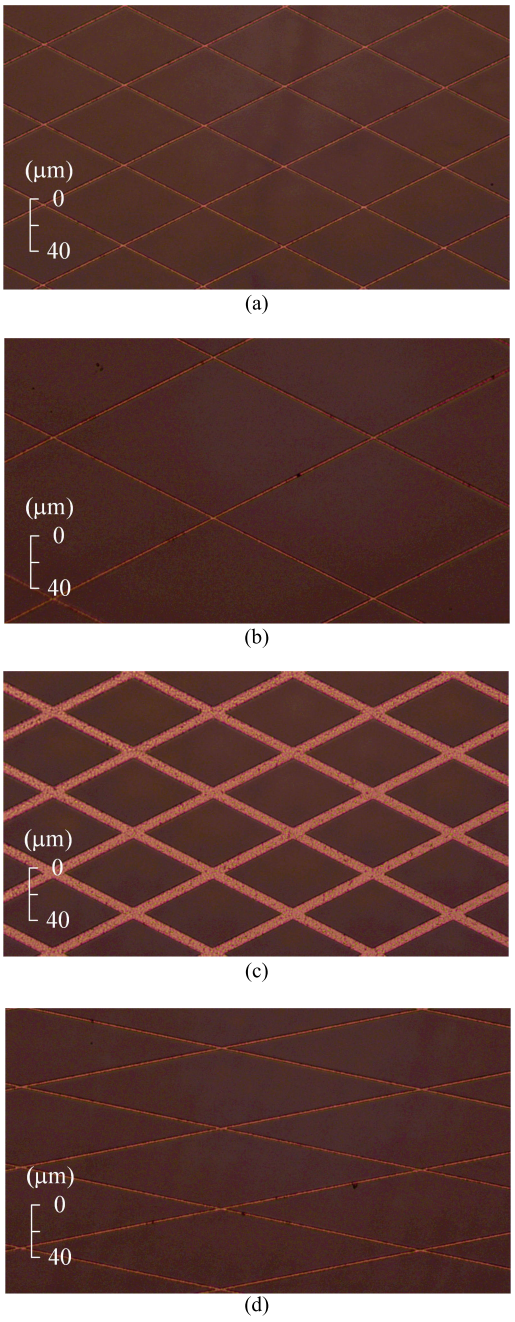

FIGURE 9. Microscopic view of the fabricated thin-metal lines corresponding to suggested methods. (a) Method 1. ($N_{mesh} = 7$). (b) Method 2. ($N_{group} = 2$). (c) Method 3. ($W_{mesh} = 7\ \mu$m). (d) Method 4. ($R_{mesh} = 5$).

$Z_0^{(0)}$, $Z_0^{(1)}$, $Z_0^{(2)}$, β_0, β_1, and β_2 due to the geometric symmetry. Thus, it is assumed that the properties of GCPWs and impedance transformers, i.e., $Z_0^{(0)}$, $Z_0^{(1)}$, β_0, and β_1, are ideal, and $Z_0^{(2)}$ is calculated by equating $Z_0^{(5)}$ to Z_{in}^{mea}, as listed in Table 1. Note that Z_{in}^{mea} is obtained from measured scattering parameter S_{11}^{mea} as

$$Z_{in}^{mea} = \frac{1 + S_{11}^{mea}}{1 - S_{11}^{mea}} \times 50 \tag{13}$$

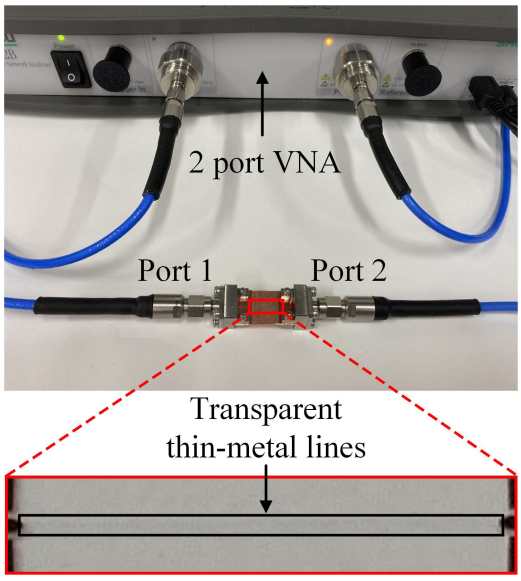

FIGURE 10. Photograph of measuring S-parameters of the fabricated transmission lines by VNA and magnified view of the sample.

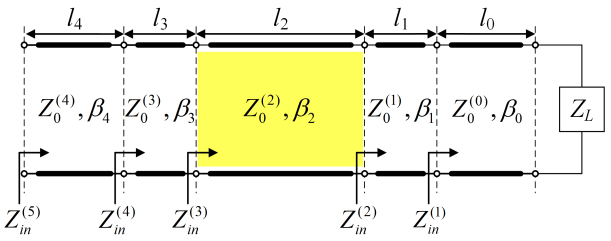

FIGURE 11. Schematic representation of the designed transmission lines with stepped characteristic and input impedances.

TABLE 1. Procedure of obtaining measured characteristic impedances.

	Initialization
Step. 1	set $Z_L = 50$, $Z_{in}^{(0)} = Z_L$ and $i = 0$.
	Update
Step. 2	calculate $Z_{in}^{(i+1)}$ by using (14) and update $i = i + 1$.
Step. 3	while if $i < 5$, go to Update and repeat Step. 2.
Step. 4	end while
Step. 5	stop and set $Z_{in}^{(i)} = Z_{in}^{(mea)}$ as (15).
Step. 6	solve (15) for $Z_0^{(2)}$ and return $Z_0^{(2)}$.

Figs. 12(a) and 12(b) present variations of both simulated and measured characteristic impedances that are adjusted by Methods 1 and 2, respectively. Both results show similar trends of decreasing Z_0 as W becomes greater, and the measured data also confirm that a larger size of unit meshes in Method 2 increases Z_0 for the same W, as discussed in Section II-B. Note that the difference between simulation and measurement tends to be larger for narrower trace widths, especially when $N_{mesh} = 1$, because a narrow transmission line with one or two unit meshes, i.e., $N_{mesh} \leq 2$, are more sensitive to geometric error in fabrication.

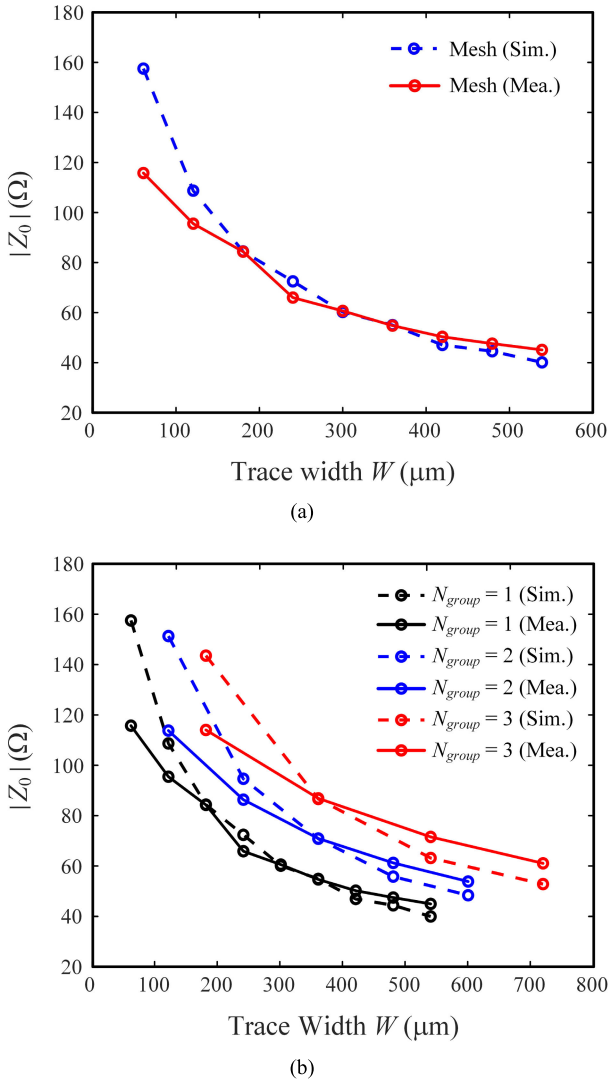

FIGURE 12. Simulated and measured variation of Z_0 of thin-metal mesh transmission lines according to trace width W for (a) Method 1 (fixing $N_{group} = 1$; $W_{mesh} = 1$ μm; $R_{mesh} = 2$) (b) Method 2 (fixing $W_{mesh} = 1$ μm; $R_{mesh} = 2$).

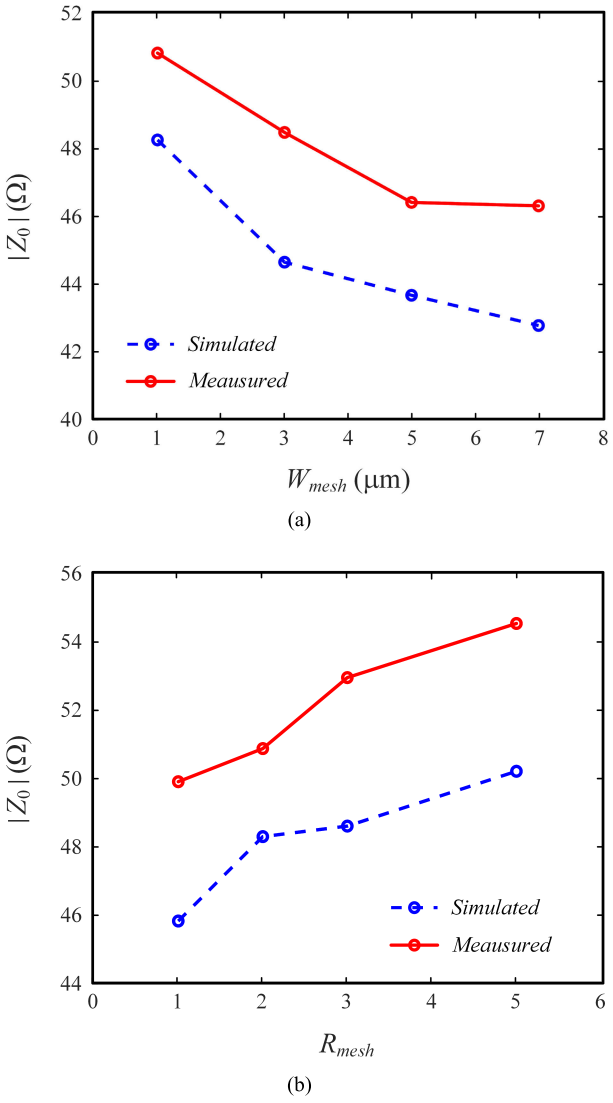

FIGURE 13. Simulated and measured variation of Z_0 of thin-metal mesh transmission lines according to thin-metal line width for (a) Method 3 (fixing $N_{mesh} = 7$; $N_{group} = 1$; $R_{mesh} = 2$) and aspect ratio of meshes for (b) Method 4 (fixing $N_{mesh} = 7$; $N_{group} = 1$; $W_{mesh} = 1$ μm).

Figs. 13(a) and 13(b) demonstrate micro-tunability of Z_0 according to W_{mesh} and R_{mesh}, respectively. The fabricated samples have almost identical W of about 420 μm, so that $Z_0^{correct}$ is primarily attributed by ρ. As expected, increasing W_{mesh} lowers Z_0, whereas Z_0 increases when R_{mesh} becomes greater. Although measured values are slightly greater than the simulation, four fabricated samples of each method are still capable of precisely tuning Z_0 as four distinguished impedances within the range of about 4 Ω.

C. APPLICATION TO DISPLAY-INTEGRATED ANTENNAS

The feasibility of the proposed methods is verified by extending applications to display-integrated antennas, and an optically transparent patch antenna operating at 28 GHz is designed by using thin-metal rhombus meshes. Fig. 14(a) presents a photograph of the fabricated antenna with the transparency of $T = 96\%$, and Fig. 14(b) presents microscopic views of the antenna structures designed by using Method 1. A quarter-wave transformer with Z_{02} is inserted between the input transmission line and the patch element to minimize the reflection coefficient, and the characteristic impedances of each section are adjusted as $Z_{01} = 47$ Ω, $Z_{02} = 60.3$ Ω, and $Z_A = 78.7$ Ω by varying the number of meshes.

Fig. 15 shows measured reflection coefficients of the thin-metal mesh antenna in comparison with simulated results to validate the effectiveness of our approach. The simulated and measured 10-dB matching bandwidths are 1.01 GHz (27.83 GHz ≤ frequency ≤ 28.84 GHz) and 0.94 GHz (27.88 GHz ≤ frequency ≤ 28.82 GHz), respectively, which

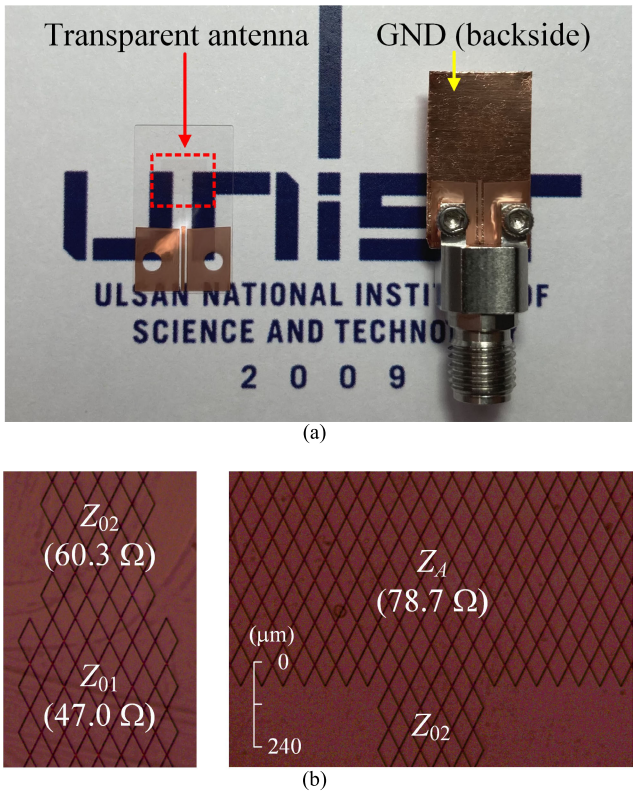

FIGURE 14. Photograph of (a) the fabricated optically transparent antenna and (b) zoomed-in view of antenna structure with the designed characteristic and antenna impedances.

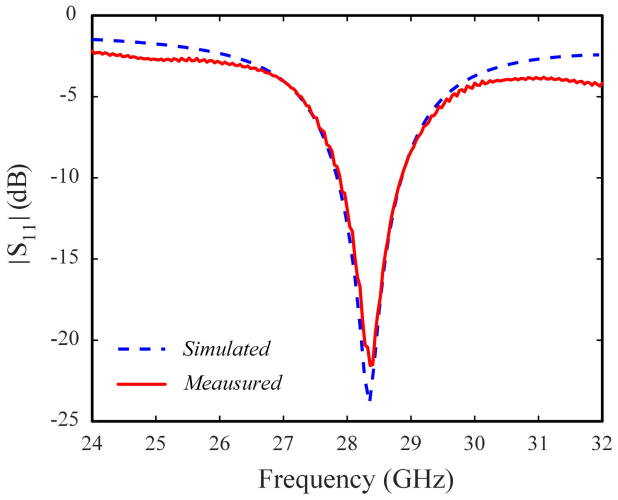

FIGURE 15. Simulated and measured reflection coefficients of the optically transparent antenna.

shows an excellent agreement with each other. The boresight gain is measured by the gain-transfer method in a semi-anechoic chamber [32], and the measured results are shown in Fig. 16. The measured and simulated peak gains are 1.7 dBi and 1.2 dBi at 28.36 GHz and 28.40 GHz, which supports that the proposed methods can provide accurate modeling for display-integrated antennas.

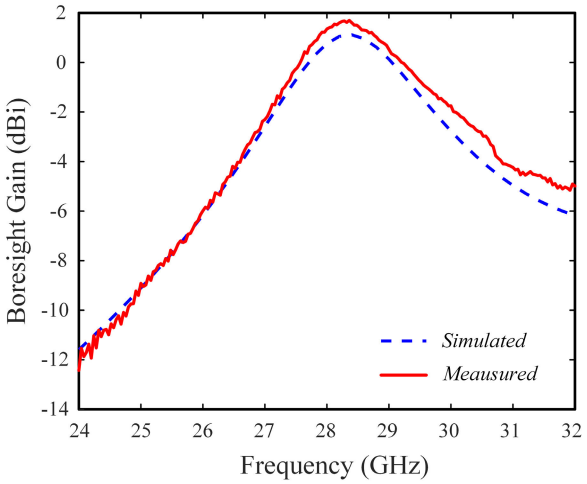

FIGURE 16. Simulated and measured gain response of the optically transparent antenna.

IV. CONCLUSION

We have investigated the four methods of adjusting characteristic impedances with empirical formulas for thin-metal mesh transmission lines. It has been confirmed that the empirical formulas can estimate accurate characteristic impedances for different geometric parameters, and the effectiveness of the proposed methods was verified by measuring characteristic impedances of the fabricated thin-metal mesh transmission lines. For further verification, the thin-metal mesh antenna was also designed to operate at 28 GHz, and its impedance matching and radiating properties were measured in the anechoic chamber. The measured results confirmed that Methods 1 and 2 provide maximum Z_0 variations of about 30 Ω in the range between $W = 181$ μm to $W = 541$ μm, and Methods 3 and 4 are suitable for precise adjustment at discrete impedances. In addition, the fabricated antenna showed good matching properties of −22 dB with the peak gain of 1.7 dBi at 28.36 GHz. We think that the proposed methods and formulas can provide accurate and flexible design rules, which will allow for potential advances in display-integrated antenna applications.

REFERENCES

[1] A. B. Smolders, A. Dubok, N. M. Tessema, Z. Chen, A. Al Rawi, U. Johannsen, T. Bressner, D. Milosevic, H. Gao, E. Tangdiongga, G. Gerini, P. G. M. Baltus, M. Geurts, and A. M. J. T. Koonen, "Building 5G millimeter-wave wireless infrastructure: Wide-scan focal-plane arrays with broadband optical beamforming," *IEEE Antennas Propag. Mag.*, vol. 61, no. 2, pp. 53–62, Apr. 2019.

[2] M. Khalily, R. Tafazolli, P. Xiao, and A. A. Kishk, "Broadband mm-wave microstrip array antenna with improved radiation characteristics for different 5G applications," *IEEE Trans. Antennas Propag.*, vol. 66, no. 9, pp. 4641–4647, Sep. 2018.

[3] R. Hosono, Y. Uemichi, Y. Hasegawa, Y. Nakatani, K. Kobayashi, and N. Guan, "Development of millimeter-wave devices based on liquid crystal polymer (LCP) substrate," *IEICE Electron. Exp.*, vol. 14, no. 20, Apr. 2017, Art. no. 20172001.

[4] E. Park and S. Kim, "Design and analysis of a TEM mode rectangular coaxial waveguide for mobile 5G millimeter wave antenna module applications," *J. Electromagn. Eng. Sci.*, vol. 20, no. 3, pp. 169–175, Jul. 2020.

[5] H. Wang and I. Park, "Characteristics of the angled printed dipole array antenna with different numbers of dipole elements," *J. Electromagn. Eng. Sci.*, vol. 20, no. 3, pp. 183–189, Jul. 2020.

[6] G. R. MacCartney, J. Zhang, S. Nie, and T. S. Rappaport, "Path loss models for 5G millimeter wave propagation channels in urban microcells," in *Proc. IEEE Global Commun. Conf. (GLOBECOM)*, Dec. 2013, pp. 3948–3953.
[7] W. Hong, K.-H. Baek, Y. Lee, Y. Kim, and S.-T. Ko, "Study and prototyping of practically large-scale mmWave antenna systems for 5G cellular devices," *IEEE Commun. Mag.*, vol. 52, no. 9, pp. 63–69, Sep. 2014.
[8] J. Zhang, X. Ge, Q. Li, M. Guizani, and Y. Zhang, "5G millimeter-wave antenna array: Design and challenges," *IEEE Wireless Commun.*, vol. 24, no. 2, pp. 106–112, Apr. 2017.
[9] W.-J. Wu, X.-F. Song, L.-R. Zhang, L. Zhou, M. Xu, L. Wang, and J.-B. Peng, "A highly stable biside gate driver integrated by IZO TFTs," *IEEE Trans. Electron Devices*, vol. 61, no. 9, pp. 3335–3338, Sep. 2014.
[10] C.-L. Lin, F.-H. Chen, W.-C. Ciou, Y.-W. Du, C.-E. Wu, and C.-E. Lee, "Simplified gate driver circuit for high-resolution and narrow-bezel thin-film transistor liquid crystal display applications," *IEEE Electron Device Lett.*, vol. 36, no. 8, pp. 808–810, Aug. 2015.
[11] J. Park, S. Y. Lee, J. Kim, D. Park, W. Choi, and W. Hong, "An optically invisible antenna-on-display concept for millimeter-wave 5G cellular devices," *IEEE Trans. Antennas Propag.*, vol. 67, no. 5, pp. 2942–2952, May 2019.
[12] W. Hong, S. Lim, S. Ko, and Y. G. Kim, "Optically invisible antenna integrated within an OLED touch display panel for IoT applications," *IEEE Trans. Antennas Propag.*, vol. 65, no. 7, pp. 3750–3755, Jul. 2017.
[13] S. Y. Lee, D. Choi, Y. Youn, and W. Hong, "Electrical characterization of highly efficient, optically transparent nanometers-thick unit cells for antenna-on-display applications," in *IEEE MTT-S Int. Microw. Symp. Dig.*, Jun. 2018, pp. 1043–1045.
[14] J. Park, S. Y. Lee, Y. Kim, J. Lee, and W. Hong, "Hybrid antenna module concept for 28 GHz 5G beamsteering cellular devices," in *IEEE MTT-S Int. Microw. Symp. Dig.*, Apr. 2018, pp. 1–3.
[15] W. Hong, J. Choi, D. Park, M.-S. Kim, C. You, D. Jung, and J. Park, "MmWave 5G NR cellular handset prototype featuring optically invisible beamforming antenna-on-display," *IEEE Commun. Mag.*, vol. 58, no. 8, pp. 54–60, Aug. 2020.
[16] A. S. Thampy and S. K. Dhamodharan, "Performance analysis and comparison of ITO- and FTO-based optically transparent terahertz U-shaped patch antennas," *Phys. E, Low-dimensional Syst. Nanostruct.*, vol. 66, pp. 52–58, Feb. 2015.
[17] S. Hong, Y. Kim, and C. Won Jung, "Transparent microstrip patch antennas with multilayer and metal-mesh films," *IEEE Antennas Wireless Propag. Lett.*, vol. 16, pp. 772–775, 2017.
[18] R. B. Green, M. Guzman, N. Izyumskaya, B. Ullah, S. Hia, J. Pitchford, R. Timsina, V. Avrutin, U. Ozgur, H. Morkoc, N. Dhar, and E. Topsakal, "Optically transparent antennas and filters: A smart city concept to alleviate infrastructure and network capacity challenges," *IEEE Antennas Propag. Mag.*, vol. 61, no. 3, pp. 37–47, Jun. 2019.
[19] M. A. H. Khan, S. Ali, J. Bae, and C. H. Lee, "Inkjet printed transparent and bendable patch antenna based on polydimethylsiloxane and Indium Tin oxide nanoparticles," *Microw. Opt. Technol. Lett.*, vol. 58, no. 12, pp. 2884–2887, Dec. 2016.
[20] K. K. So, B.-J. Chen, and C. H. Chan, "Microwave and millimeter-wave MIMO antenna using conductive Ito film," *IEEE Access*, vol. 8, pp. 207024–207033, 2020.
[21] H. Jae Song, T. Yuan Hsu, D. F. Sievenpiper, H. Pin Hsu, J. Schaffner, and E. Yasan, "A method for improving the efficiency of transparent film antennas," *IEEE Antennas Wireless Propag. Lett.*, vol. 7, pp. 753–756, 2008.
[22] J. Hautcoeur, L. Talbi, and K. Hettak, "Feasibility study of optically transparent CPW-fed monopole antenna at 60-GHz ISM bands," *IEEE Trans. Antennas Propag.*, vol. 61, no. 4, pp. 1651–1657, Apr. 2013.
[23] P. Duy Tung and C. W. Jung, "Optically transparent wideband dipole and patch external antennas using metal mesh for UHD TV applications," *IEEE Trans. Antennas Propag.*, vol. 68, no. 3, pp. 1907–1917, Mar. 2020.
[24] S. Sheikh, "Circularly polarized meshed patch antenna," *IEEE Antennas Wireless Propag. Lett.*, vol. 15, pp. 352–355, 2016.
[25] S. H. Kang and C. W. Jung, "Transparent patch antenna using metal mesh," *IEEE Trans. Antennas Propag.*, vol. 66, no. 4, pp. 2095–2100, Apr. 2018.
[26] T. W. Turpin and R. Baktur, "Meshed patch antennas integrated on solar cells," *IEEE Antennas Wireless Propag. Lett.*, vol. 8, pp. 693–696, 2009.
[27] V. K. Khanna, *Fundamentals of Solid-State Lighting: LEDs, OLEDs, and Their Applications in Illumination and Displays*. Boca Raton, FL, USA: CRC Press, 2014.
[28] S. Lee, M. Choo, S. Jung, and W. Hong, "Optically transparent nanopatterned antennas: A review and future directions," *Appl. Sci.*, vol. 8, no. 6, p. 901, May 2018.
[29] Z. J. Silva, C. R. Valenta, and G. D. Durgin, "Design and characterization of meshed microstrip transmission lines," in *IEEE MTT-S Int. Microw. Symp. Dig.*, Jun. 2019, pp. 811–814.
[30] D. M. Pozar, *Microwave Engineering*, 4th ed. Nashville, TN, USA: Wiley, 2012, pp. 56–161.
[31] D. J. Resnick, W. J. Dauksher, D. Mancini, K. J. Nordquist, T. C. Bailey, S. Johnson, N. Stacey, J. G. Ekerdt, C. G. Willson, S. V. Sreenivasan, and N. Schumaker, "Imprint lithography for integrated circuit fabrication," *J. Vac. Sci. Technol. B, Microelectron. Nanometer Struct.*, vol. 21, no. 6, p. 2624, 2003.
[32] C. A. Balanis, *Antenna Theory: Analysis and Design*, 4th ed. Hoboken, NJ, USA: Wiley-Blackwell, 2016, pp. 1006–1010.

JIN MYEONG HEO received the B.S. degree in electrical and computer engineering from the Ulsan National Institute of Science and Technology (UNIST), Ulsan, South Korea, in 2019, where he is currently pursuing the combined M.S./Ph.D. degree in electrical engineering. His research interests include display-integrated antennas, optically transparent antennas/transmission lines, and beamforming array antennas.

EUN JIN SUNG received the B.S. degree in computer science engineering from Dongguk University, Seoul, South Korea, in 2013. She is currently a Staff Engineer with Samsung Display. Her research interests include display-integrated antennas and optically transparent antenna with high-gain and broadband.

JAE KYOUNG KIM received the B.S. degree in electrical engineering from Dongguk University, Seoul, South Korea, in 2005. He is currently a Principal Engineer with Samsung Display. His research interests include next generation display and sensing technology for display.

GANGIL BYUN (Member, IEEE) received the B.S. and M.S. degrees in electronic and electrical engineering from Hongik University, Seoul, South Korea, in 2010 and 2012, respectively, and the Ph.D. degree in electronics and computer engineering from Hanyang University, Seoul, in 2015. After his graduation, he returned to Hongik University to work as a Research Professor and performed active research for a period of two years. He joined the Faculty of the Ulsan National Institute of Science and Technology (UNIST), in February 2018, where he is currently an Assistant Professor of electrical engineering (EE). He has actively contributed to the improvement of overall beamforming performances by combining both antenna engineering and signal processing perspectives. His research interests include the design and analysis of small antenna arrays for adaptive beamforming applications, such as direction of arrival estimation, interference mitigation, and radar. His recent research interests include high-Q metasurfaces, optically invisible antennas, and waveguide slot array antennas to bring advances in future wireless communications systems.